Hindawi
Mathematical Problems in Engineering
Volume 2020, Article ID 2614574, 13 pages
https://doi.org/10.1155/2020/2614574

Research Article

Scattering of SH Waves by a Partially Debonded Cylindrical Inclusion in the Covering Layer

Hui Qi, Yang Zhang, Fuqing Chu, and Jing Guo

College of Aerospace and Civil Engineering, Harbin Engineering University, Harbin 150001, China

Correspondence should be addressed to Yang Zhang; zhangyang1987@hrbeu.edu.cn

Received 18 January 2020; Revised 5 May 2020; Accepted 7 May 2020; Published 30 May 2020

Academic Editor: Leandro F. F. Miguel

This article presents analytical solutions to the problem of dynamic stress concentration and the surface displacement of a partially debonded cylindrical inclusion in the covering layer under the action of a steady-state horizontally polarized shear wave (SH wave); these solutions are using the complex function method and wave function expansion method. By applying the large-arc assumption method, the straight line boundary of the half-space covering layer is transformed into a curved boundary. The wave field of the debonded inclusion is constructed utilizing a Fourier series and boundary conditions of continuity. The impact of debonding upon the dynamic stress concentration and surface displacement around the cylindrical concrete or steel inclusion is analyzed through numerical examples of the SH waves that are incident at normal angles, from a harder medium to a softer medium and from a softer medium to a harder medium. The examples show that various factors (including the medium parameters of the soil layers and the inclusion, the frequency of the incident waves, and the debonding situations) jointly affect the dynamic stress concentration factor and the surface displacement around the structure.

1. Introduction

The development and utilization of underground space is an important factor to consider when seeking to optimize the urban spatial structure and ease the strain on urban land resources. Ensuring the safety of underground structures during an earthquake is vital for protecting people's lives and property. Various wave fields around the underground structure will interact and interfere with each other, which make analyzing the dynamic response of the underground structure very complicated; this has caused widespread concern among scholars [1]. Stress concentration refers to the phenomenon of a local increase in stress in an object, which has a very important relationship with the damage inflicted on a structure during an earthquake. Studies have revealed that, during an earthquake, the dynamic stress concentration around an underground tunnel is attributed to the multiple scattering of seismic waves by the earth's surface and cavities [2]. Because of factors such as construction technology, soil settlement, and changes in the groundwater level, at some parts of the structure, it will veer away from the interface between itself and the surrounding soil medium, forming a debonded area. The existence of debonding both causes a dramatic change in the dynamic stress concentration at the edges of the structure and has a substantial impact on the ground surface vibration at the same time; consequently, this affects the nearby buildings. Therefore, it has become necessary to study the impact of this debonding. In engineering, when studying various mechanical problems, the earth is often regarded as a whole elastic half space. Thus far, the research results regarding horizontally polarized shear wave (SH wave) scattering in full space and half space are plentiful [2]. However, when the ground is considered to consist of multiple soil layers, the boundary conditions become more complicated, and this means that the mirror method, which is often used in the study of SH wave scattering in a half space, is no longer applicable. Furthermore, in reality, each soil layer often has different mechanical properties, which will make it more difficult to model and thus solve. Scholars from various countries have not yet devised an ideal method for solving such problems, and their research has only encompassed the

problem of elastic wave scattering in the covering layer of specific terrain [3, 4]. From the perspective of engineering applications, in this paper, we consider comprehensively the material differences in various soil layers and structures and try to obtain a solution to the problem of dynamic stress concentration and the surface displacement of SH waves scattered by the debonded structure in the covering layer, thus providing a theoretical reference for seismic design in engineering. Therefore, the impact of seismic waves on a structure can be reduced by means of changing materials, changing dimensions, and strengthening weak areas, which has extensive practical significance for tunnel engineering and mining engineering.

In 1961, Baron used the integral transform method and wave function expansion method to provide an analytical solution to the compressional wave pulse scattering problem for a cylindrical cavity [5]. Following this, Mow and Mente studied the scattering of shear waves by a cylinder [6]. Liu et al. solved successfully the dynamic stress concentration problem with respect to cavities of arbitrary shape in 1982, and they applied the complex variable function method to the two-dimensional elastic dynamics scattering problem [7]. They also used the complex function method and moving coordinate method effectively to solve the problem of the scattering of SH waves by shallowly buried structures in a half space [8, 9]. Successively, Qi and Yang have extended this into the areas of half space, half-space interface, circular cavities in half-space bidirectional media, and inclusion [10, 11]. The debonding of a structure can be considered to be a crack without surface contact. In the 1980s, Coussy studied the case where a cylindrical inclusion and the substrate were debonded [12]. In the 1990s, Yang and Norris studied the condition of a single-arc crack and provided near-field and far-field solutions at arbitrary wavelengths [13, 14]. Wang analyzed and solved the problem of plane-wave scattering by a partially detached, rigid, or elastic cylindrical inclusion, based on the wave function expansion method [15, 16]. In 2008, Yang revealed the finite element numerical results of the transient response of an infinite half space to a covering layer crack under the action of SH waves [17]. At the end of the 20th century, Lee and Karl used the large-arc assumption method to turn the traditional straight boundary problem into a curved boundary problem, and they devised analytical solutions for the scattering of the primary waves and other shear waves by a single circular cavity [18–21]. Recently, Fang et al. [22–24] investigated the interface effect in the propagation and diffraction of elastic waves.

In addition, the theory of elastic waves also has a great value in engineering applications, such as fatigue failure of structural materials [25–27] due to cyclic strain of the loading waves. In this paper, the concrete and steel structures commonly used in engineering have been selected as the research objects, and they are each regarded as a cylindrical inclusion in the covering layer. On the basis of the large-arc assumption, we transform the straight boundary of two soil layers into a curved (or arc) boundary to construct a scattered wave field in each soil layer. We then decompose the model into circular cavity scattering and inclusion scattering problems in the covering layer using the cutting method. The conjunction between the two is then applied to the common boundary, and the wave field of the debonded inclusion is constructed using a Fourier series and continuous boundary conditions, which avoids the processing of singular points on the edges of the debonded structure and obtains an analytical solution for the problem. Moreover, in the numerical programming calculations used, unlike in the standard literature, this paper does not only perform theoretical derivation and idealized parameter selection but also provides the actual material parameters of the soil layers and inclusion based on actual engineering. The problems of the dynamic stress concentration and the surface displacement surrounding debonded inclusion are analyzed comprehensively in two typical geological combinations: SH wave propagation from a harder medium to a softer medium and from a softer medium to a harder medium.

2. Theoretical Model and Fundamental Equations

A two-dimensional model of a single cylindrical debonded inclusion in the covering layer is shown in Figure 1. The lower soil layer is Domain I, in which the shear velocity is c_1, the density is ρ_1, the shear modulus is μ_1, and the SH wavenumber is k_1; the upper covering layer is Domain II, in which the shear velocity is c_2, the density is ρ_2, the shear modulus is μ_2, and the SH wavenumber is k_2; and the circular inclusion in the covering layer is Domain III, in which the shear velocity is c_3, the density is ρ_3, the shear modulus is μ_3, and the SH wavenumber $i_s\ k_3$. The upper boundary of the covering layer is marked as T_U, and the lower boundary is T_D, and the boundary of the circular inclusion is T_C. The inclusion radius is r, and the thickness of the covering layer is h. The distance from the center of the circular inclusion to the upper boundary, T_u, of the covering layer is h_1 and to the lower boundary, T_D, is h_2. Using the large-arc assumption method, the upper and lower boundaries of the covering layer are approximated using concentric arcs, each with a large radius; the upper boundary, T_u, becomes T_u, and the lower boundary, T_u, becomes T_u. A rectangular coordinate system, $X_1O_1Y_1$, is established with the center of the large arc as the origin O_1; a rectangular coordinate system, $X_2O_2Y_2$, is established, with the center of the inclusion as the origin O_2, and a line parallel to the interface T_u is taken as the axis X_2 so that the axis Y_1 and the axis Y_2 are on the same straight line. The polar coordinate angle of any point in the space under the coordinate system $X_1O_1Y_1$ is θ_1, and the polar coordinate angle of any point of the inclusion boundary in the coordinate system $X_2O_2Y_2$ is θ_2. When there is debonding in the inclusion, θ_3 and θ_4 are the starting and ending angles of the debonded structure, respectively, and $\theta_4 \geq \theta_3$. The steady-state SH wave is incident from Domain I, with an incident angle of α_0.

In this paper, we study the scattering of SH waves in out-of-plane shear motion. The steady-state SH wave displacement field $W(X, Y)$ excited by a half space satisfies the Helmholtz equation [7]:

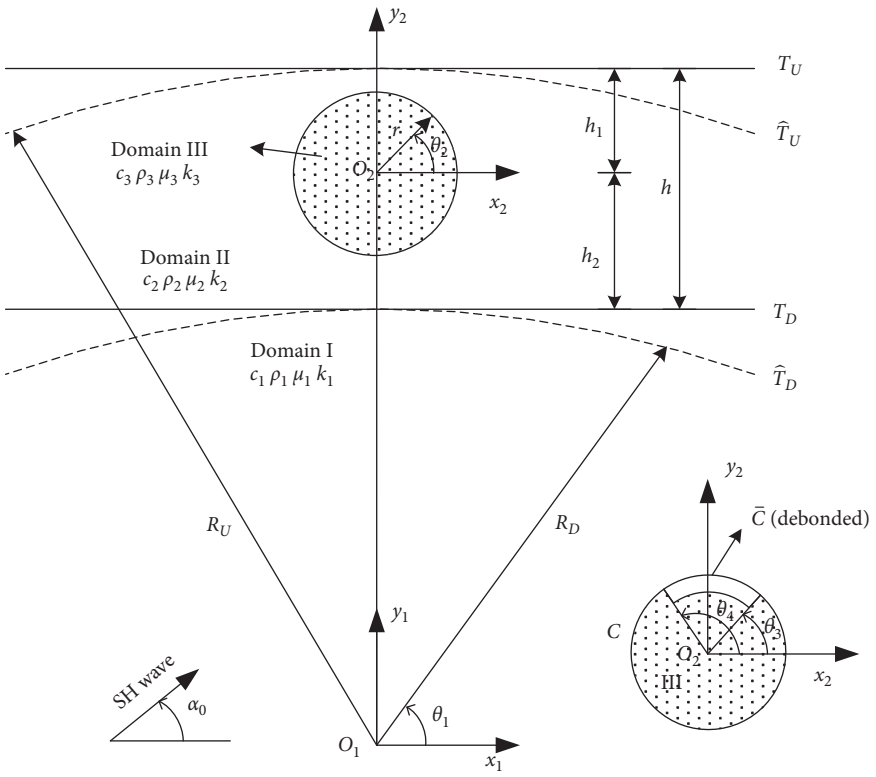

Figure 1: Schematic diagram of the layer half space.

$$\frac{\partial^2 W}{\partial X^2}+\frac{\partial^2 W}{\partial Y^2+k^2 W}=0, \tag{1}$$

in which k is the wavenumber and $k=\omega/c$; ω is the circular frequency of the displacement field $W(X,Y)$; and c is wave velocity and $c=\sqrt{G/\rho}$, in which G and ρ are the shear modulus and density of the medium, respectively. The complex variable functions $z_s=X_s+iY_s$ and $\overline{z}_s=X_s-iY_s$ are introduced, where $S=1,2$ and the complex planes $(z_1,\overline{z}_1)$ and $(z_2,\overline{z}_2)$ corresponding to the coordinate systems $X_1O_1Y_2$ and $X_2O_2Y_2$, respectively, are established. The relationship of each geometric variable is as follows:

$$\begin{aligned} h&=h_1+h_2,\\ R_U&=h+R_D,\\ z_2&=z_1-i(R_D+h_2). \end{aligned} \tag{2}$$

In the complex plane, (1) can be expressed as follows:

$$\frac{4\partial^2 W}{\partial z\partial\overline{z}+k^2 W}=0. \tag{3}$$

In a complex plane polar coordinate system, the stress-strain relationship is as follows:

$$\begin{aligned} \tau_{z\rho}&=G\left[\left(\frac{\partial W}{\partial z}\right)\left(\frac{z}{|z|}\right)+\left(\frac{\partial W}{\partial\overline{z}}\right)\left(\frac{|z|}{z}\right)\right],\\ \tau_{z\varphi}&=iG\left[\left(\frac{\partial W}{\partial z}\right)\left(\frac{z}{|z|}\right)-\left(\frac{\partial W}{\partial\overline{z}}\right)\left(\frac{|z|}{z}\right)\right]. \end{aligned} \tag{4}$$

2.1. Wave Fields. In plane $(z_1,\overline{z}_1)$, the displacement field of the incident wave in Domain I is as follows [7]:

$$W^{(i)}_{(z_1,\overline{z}_1)}=W_0\exp\left[ik_1\mathrm{Re}\left(z_1e^{-i\alpha_0}\right)\right]. \tag{5}$$

In plane $(z_1,\overline{z}_1)$, the displacement field of the scattered wave generated in Domain I by the boundary T_D can be divided into two parts of $W^{(S1)}_{(z_1,\overline{z}_1)}$ and $W^{(S2)}_{(z_1,\overline{z}_1)}$ as follows [7]:

$$\begin{aligned} W^{(S1)}_{(z_1,\overline{z}_1)}&=\sum_{n=-\infty}^{n=+\infty}A_nH_n^{(2)}\left(\frac{k_1}{|z_1|}\right)\left(\frac{z_1}{|z_1|}\right)^n,\\ W^{(S2)}_{(z_1,\overline{z}_1)}&=\sum_{n=-\infty}^{n=+\infty}B_nH_n^{(1)}\left(\frac{k_2}{|z_1|}\right)\left(\frac{z_1}{|z_1|}\right)^n. \end{aligned} \tag{6}$$

In addition, in plane $(z_2,\overline{z}_2)$,$W^{(S2)}_{(z_1,\overline{z}_1)}$ is expressed as follows:

$$W^{(S2)}_{(z_2,\overline{z}_2)}=\sum_{n=-\infty}^{n=+\infty}B_nH_n^{(1)}\left(k_2|z_{2+}|\right)\left(\frac{z_{2+}}{|z_{2+}|}\right)^n, \tag{7}$$

in which $Z_{2+}=z_2+i(R_D+h_2)$.

In plane $(z_2,\overline{z}_2)$, the displacement field of the scattered wave generated in the Domain I by the boundary T_C can be divided into two parts of $W^{(S3)}_{(z_2,\overline{z}_2)}$ and $W^{(S4)}_{(z_1,\overline{z}_1)}$.

The former is as follows:

$$W^{(S3)}_{(z_2,\overline{z}_2)}=\sum_{n=-\infty}^{n=+\infty}C_nH_n^{(1)}\left(\frac{k_2}{|z_2|}\right)\left(\frac{z_2}{|z_2|}\right)^n. \tag{8}$$

In addition, in plane $(z_1,\overline{z}_1)$, it is expressed as follows:

$$W_{(z_1,\overline{z}_1)}^{(S3)} = \sum_{n=-\infty}^{n=+\infty} C_n H_n^{(1)}\left(k_2|z_{1-}|\right)\left(\frac{z_{1-}}{|z_{1-}|}\right)^n, \tag{9}$$

in which $Z_{1-} = z_1 - i(R_D + h_2)$.

In plane $(z_1, \overline{z}_1)$, the latter is as follows:

$$W_{(z_1,\overline{z}_1)}^{(S4)} = \sum_{n=-\infty}^{n=+\infty} D_n H_n^{(2)}\left(\frac{k_2}{|z_1|}\right)\left(\frac{z_1}{|z_1|}\right)^n. \tag{10}$$

In addition, in plane $(z_2, \overline{z}_2)$, it is expressed as follows:

$$W_{(z_2,\overline{z}_2)}^{(S4)} = \sum_{n=-\infty}^{n=+\infty} D_n H_n^{(2)}\left(k_2|z_{2+}|\right)\left(\frac{z_{2+}}{|z_{2+}|}\right)^n. \tag{11}$$

In the complex plane $(z_2, \overline{z}_2)$, the standing wave $W^{(ST)}$ generated by the circular inclusion T_C in Domain III of the covering layer satisfies both stress freedom on the boundary $\overline{C}$, and displacement and stress continuity on the boundary C:

$$\tau_{Z\rho,(Z_2,\overline{Z}_2)}^{(ST)} = \left\{ \begin{array}{ll} 0 & \overline{Z}_2 \in C \\ 0.5W_3\mu_3 k_3 \sum_{n=-\infty}^{n=+\infty} E_n\left[J_{l-1}\left(K_3|Z_2|\right) - J_{l+1}\left(K_3|z_2|\right)\right]\left(z_2/|z_2|\right)^n & Z_2 \in C \end{array} \right\}. \tag{12}$$

The standing wave corresponding to (12) is as follows:

$$W_{(r_2+\overline{r})_2}^{(ST)} = W_3 \sum_{L=-\infty}^{L=+\infty} F_1 J_1\left(K_3|z_2|\right)\left(\frac{|z_2|}{|z_2|}\right)^l, \tag{13}$$

$$\tau_{z\rho,(z_2,\overline{z}_2)}^{(ST)} = 0.5W_3\mu_3 k_3 \sum_{n=-\infty}^{n=+\infty} F_1\left[J_{l-1}\left(K_3|z_2|\right) - J_{l+1}\left(K_3|z_2|\right)\right]\left(\frac{z_2}{|z_2|}\right)^l, \tag{14}$$

where E_n and F_1 are undetermined coefficients and W_3 is the maximum amplitude of a standing wave, which is set to $W_3 = 1$ in this paper.

Expanding the previous formula (12) into a (10), Fourier series in $[-\pi, +\pi]$ gives the following:

$$\tau_{z\rho,(z_2,\overline{z}_2)}^{(ST)} = 0.5W_3\mu_3 k_3 \sum_{l=-\infty}^{l=+\infty}\sum_{l=-\infty}^{l=+\infty} a_{\ln} E_n\left[J_{n-1}\left(K_3|Z_2|\right) - J_{n+1}\left(K_3|Z_2|\right)\right]\left(\frac{z_2}{|z_2|}\right)^l, \tag{15}$$

in which

$$a_{\ln} = \frac{1}{2\prod}\int_{\theta_4-2\pi}^{\theta_3} e^{i(n-l)\theta}d\theta = \left\{ \begin{array}{ll} \dfrac{2\pi + (\theta_3 - \theta_4)}{2\pi} & (l = n) \\ \dfrac{e^{i(n-1)\theta_3} - e^{i(n-1)\theta_4}}{2\pi i(n-l)} & (l \neq n) \end{array} \right\}. \tag{16}$$

In complex plane $(z_2, \overline{z}_2)$, θ_3 and θ_4 are the starting and ending angles of the debonded structure, respectively, and $\theta_4 \geq \theta_5$.

On comparing (15) and (14) with $|z_2| = R$, we obtain the following:

$$F_l = W_3 \sum_{n=-\infty}^{n=+\infty} a_{\ln}\frac{J_{n-1}(k_3R) - J_{n+1}(k_3R)}{J_{l-1}(k_3R) - J_{n-1}(k_3R)}E_n. \tag{17}$$

By replacing (13) with (17), we determine the standing wave in the inclusion:

$$W_{(z_2,\overline{z_2})}^{(ST)} = \sum_{l=-\infty}^{l=+\infty}\sum_{n=-\infty}^{n=+\infty} E_n\frac{J_{n-1}(k_3R) - J_{n+1}(k_3R)}{J_{l-1}(k_3R) - J_{n+1}(k_3R)}a_{\ln}J_l\left(k_3|z_2|\right)\left(\frac{z_2}{|z_2|}\right)^l. \tag{18}$$

The standing wave solution in Domain III is (17), which satisfies the stress freedom on the boundary $\overline{C}$; the displacement and stress are continuous on the boundary C, and the corresponding stress expression is as follows:

$$W_{z\rho,(z_2,\overline{z_2})}^{(ST)} = 0.5\mu_3 k_3 \sum_{l=-\infty}^{l=+\infty}\sum_{n=-\infty}^{n=+\infty} E_n\frac{J_{n-1}(k_3R) - J_{n+1}(k_3R)}{J_{l-1}(k_3R) - J_{n+1}(k_3R)}a_{\ln} \cdot \left[J_{l-1}\left(k_3|z_2|\right) - J_{l+1}\left(k_3|z_2|\right)\right]\left(\frac{z_2}{|z_2|}\right)^l,$$

$$W_{z\rho,(z_2,\overline{z_2})}^{(ST)} = \frac{i\mu_3}{|z_2|}\sum_{l=-\infty}^{l=+\infty}\sum_{n=-\infty}^{n=+\infty} lE_n\frac{J_{n-1}(k_3R) - J_{n+1}(k_3R)}{J_{l-1}(k_3R) - J_{n+1}(k_3R)}a_{\ln}J_l \cdot \left(k_3|z_2|\right)\left(\frac{z_2}{|z_2|}\right)^l. \tag{19}$$

3. Boundary Conditions

The boundary conditions to be met are as follows:

(i) Continuous displacement on $T_D(|z_1| = R_D)$: $W_{(z_1,\overline{z}_1)}^{(i)} + W_{(z_1,\overline{z}_1)}^{(S1)} = W_{(z_1,\overline{z}_1)}^{(S2)} + W_{(z_1,\overline{z}_1)}^{(S3)} + W_{(z_1,\overline{z}_1)}^{(S4)}$

(ii) Continuous radial stress on $T_D(|z_1| = R_D)$: $\tau_{z\rho,(z_1,\overline{z}_1)}^{(i)} + \tau_{z\rho,(z_1,\overline{z}_1)}^{(S1)} = \tau_{z\rho,(z_1,\overline{z}_1)}^{(S2)} + \tau_{z\rho,(z_1,\overline{z}_1)}^{(S3)} + \tau_{z\rho,(z_1,\overline{z}_1)}^{(S4)}$

(iii) Continuous displacement on $T_C(|z_2| = r)$: $W_{(z_2,\overline{z}_2)}^{(S2)} + W_{(z_2,\overline{z}_2)}^{(S3)} + W_{(z_2,\overline{z}_2)}^{(S4)} = W_{(z_2,\overline{z}_2)}^{(ST)}$

(iv) Continuous radial stress on $T_C(|z_2| = r)$: $\tau_{z\rho,(z_2,\overline{z}_2)}^{(S2)} + \tau_{z\rho,(z_2,\overline{z}_2)}^{(S3)} + \tau_{z\rho,(z_2,\overline{z}_2)}^{(S4)} = \tau_{z\rho,(z_2,\overline{z}_2)}^{(ST)}$

(v) Free radial stress on $T_U(|z_1| = R_U)$: $\tau^{(S2)}_{z\rho,(z_1,\bar{z}_1)} + \tau^{(S3)}_{z\rho,(z_1,\bar{z}_1)} + \tau^{(S4)}_{z\rho,(z_1,\bar{z}_1)} = 0$

A Fourier series expansion is performed on the two ends of the equation, according to the angular variable θ, and an infinite term equation system containing infinite unknown coefficients is obtained. According to the attenuation properties of the scattered wave, the finite terms are intercepted for m and n to ensure accuracy. These boundary condition equations can be transformed into a finite term linear equation set, and the coefficients A_n, B_n, C_n, D_n, and E_n are obtained.

4. Dynamic Stress Concentration Factor and Surface Displacement Amplitudes

We define the dynamic stress concentration factor (DSCF) denoted by $\tau^*_{z\varphi,(z_2,\bar{z}_2)}$ as follows:

$$\tau^*_{z\varphi,(z_2,\bar{z}_2)} = \left| \frac{\left(\tau^{(S2)}_{z\varphi,(z_2,\bar{z}_2)} + \tau^{(S3)}_{z\varphi,(z_2,\bar{z}_2)} + \tau^{(S4)}_{z\varphi,(z_2,\bar{z}_2)}\right)}{(ik_1\mu_1 W_0)} \right|_{|z_2|=R}, \tag{20}$$

at the edge of a cylindrical inclusion, which is abbreviated as DSCF$\sigma^*_{\theta z}$, for which the maximum value is DSCF$\sigma^*_{\theta z\max}$. The DSCF represents the stress response of an elastic medium to an external load. The total wave field of the displacement in Domain II in the covering layer is $W^{(t)} = W^{(S2)} + W^{(S3)} + W^{(S4)}$. This can also be expressed as $W^{(t)} = |W^{(t)}|e^{i(\omega t-\phi)}$, in which ϕ is the phase of $W^{(t)}$, and the frequency of the incident wave ω can be combined with the radius of the circular inclusion to obtain an incident wavenumber. From $k = \omega/c$ and $\lambda = cT$, in which λ is the wavelength and c is the velocity, we can determine that the incident wavenumber is $kr = 2\pi r/\lambda$.

5. Numerical Results and Discussion

The numerical examples focus on the effects of debonding on the dynamic stress concentration and the surface displacement of a cylindrical concrete or steel inclusion when SH waves are incident vertically. We assume that the debonding position exists in the upper half of the inclusion, that is, the starting angle and the ending angle of the debonding are $\theta_3 = 0$ and $\theta_4 = \pi/2$, respectively. The incident angle of the SH wave $\alpha_0 = 90^\circ$, the depth of the cylindrical inclusion $h_1 = 1.5\,r$, radius $r = 1$, the density of Domain I $\rho_1 = 1$, the shear velocity $c_1 = 1$, and the shear modulus $\mu_1 = 1$ can be obtained from $C = \sqrt{\mu/\rho}$. For convenience and to facilitate the analysis, all parameters in this example are dimensionless. By defining the parameter combination $c^* = c_2/c_1$, $c^\# = c_3/c_1$, $\rho^* = \rho_2/\rho_1$, $\rho^\# = \rho_3/\rho_1$, $k^* = k_2/k_1$, and $k^\# = k_3/k_1$ and from $k = \omega/c$, we obtain $k^* = 1/c^* = \sqrt{\rho^*/\mu^*}$ and $k^\# = 1/c^\# = \sqrt{\rho^\#/\mu^\#}$. A value of $k^* > 1$ indicates that Domain I is "harder" than Domain II, that is, the incident wave propagates from the "harder" half space, and, at this moment, the circular inclusion is positioned in the "softer" covering layer. Two commonly used materials are applied to create the inclusion:

(1) C30 concrete, with density $\rho_3 = 2400\,\text{kg/m}^3$, shear modulus $\mu_3 = 12\,\text{GPa}$, and shear velocity $C_3 = 2240\,m/s$

(2) Q345 steel, with density $\rho_3 = 7850\,\text{kg/m}^3$, shear modulus $\mu_3 = 79\,\text{GPa}$, and shear velocity $C_3 = 3160\,m/s$

Two geological conditions are selected:

(i) SH wave incident from the harder medium to the softer medium: where, Domain I is granite of density $\rho_1 = 2800\,\text{kg/m}^3$ and shear velocity $c_1 = 3200\,\text{m/s}$, and Domain II in the covering layer is sandstone of density $\rho_2 = 2240\,\text{kg/m}^3$ and shear velocity $c_2 = 2100\,m/s$. When $\rho_1 = 1$, $\rho^* = 0.8$ and $k^* = 1.5$. When the inclusion is C30 concrete, $\rho^\# \approx 0.85$ and $k^\# \approx 1.4$. When the inclusion is Q345 steel, $\rho^\# \approx 2.8$ and $k \approx 1.0$.

(ii) SH wave incident from the softer medium to the harder medium: where, Domain I is coal of density $\rho_1 = 1500\,\text{kg/m}^3$ and shear velocity $c_1 = 1000\,\text{m/s}$, and Domain II in the covering layer is sandstone of density $\rho_2 = 2240\,\text{kg/m}^3$ and shear velocity $c_2 = 2100\,m/s$. When $\rho_1 = 1$, $\rho^* \approx 1.7$ and $K^\# \approx 0.4$. When the inclusion is C30 concrete, $\rho^\# = 1.6$ and $K^\# \approx 0.45$. When the inclusion is Q345 steel, $\rho^\# \approx 5.2$ and $K^\# \approx 0.3$.

When $\mu^* = k^* = \rho^* = 1$, the parameters of Domain I and Domain II are the same, so the boundary T_D does not exist, and Domains I and II merge into one. At this time, $\mu^* = k^* = \rho^* = 1$, and Domain III can be seen as a circular cavity without media. This degenerates into the problem of the scattering of an SH wave by a circular cavity in the half space, as illustrated in Figure 2. Figure 3 shows that when $R_d \geq 120\,r$, $k_1 = 0.1$ and h_1 are the DSCFs around the circular cavity when 1.5γ and when $12\,r$, respectively, and the results are basically consistent with the results of Figure 4 in [8]. Figure 5 identifies that when h_1 is $3\,r$ and $12\,r$, the changes in the amplitude of the horizontal surface displacement with x/r, respectively. The results are fundamentally consistent with what is demonstrated in Figures 3 and 5 in [9], that is, when $h_1 \geq 12\,r$, the DSCFs and the ground surface horizontal displacement approach a constant, which also verifies the rationality of using the large-arc assumption method.

Figure 6 illustrates the dynamic stress concentration around the concrete inclusion in the sandstone covering layer when the SH wave for geological combination A is perpendicularly incident from the granite layer to the sandstone layer. In this instance, the SH wave is incident from the harder medium to the softer medium, and the parameters are $\rho^* = 0.8$, $k^* = 1.5$, $\rho^\# \approx 0.85$, and $k^\# \approx 1.4$. When $k_1 r = 0.1$, which is a low-frequency incidence, the DSCF around the inclusion is elliptical. When the inclusion is not debonded, DSCF$\sigma^*_{\theta z\max}$ appears at about 200° and 340°. When bonded, the overall DSCF$\sigma^*_{\theta z\max}$ increases to a certain extent, but there is no obvious change in the DSCF$\sigma^*_{\theta z}$

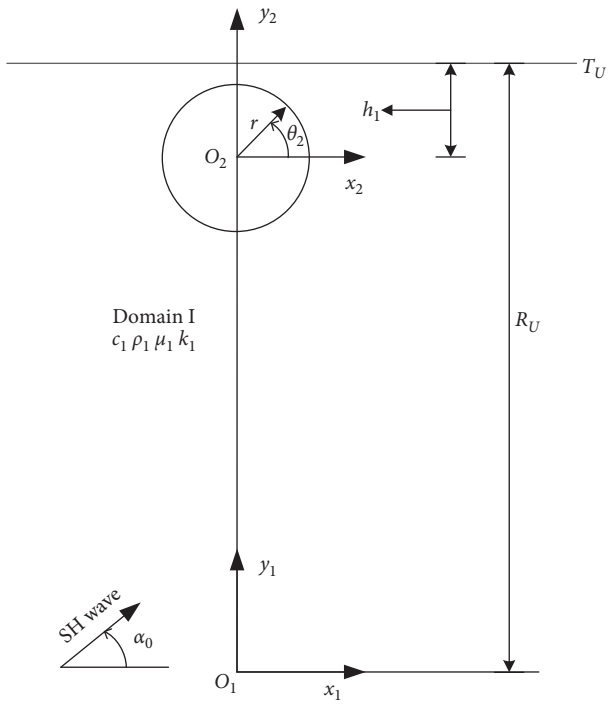

Figure 2: Schematic diagram of the half-space modification.

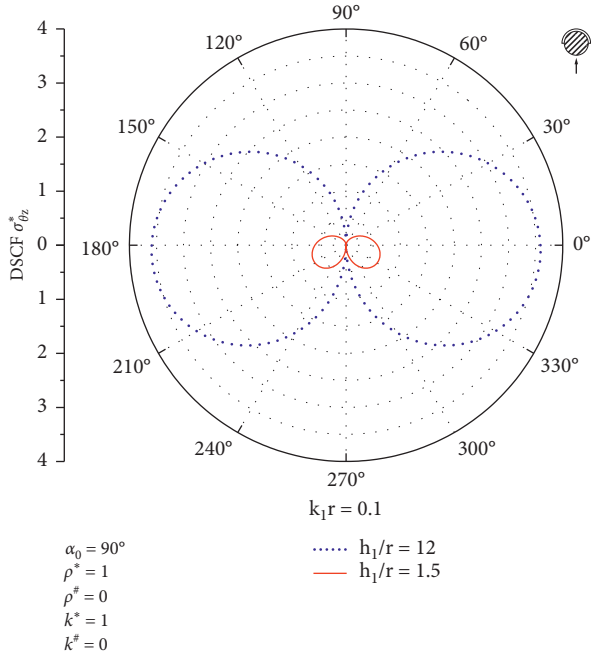

Figure 3: $DSCF\sigma^*_{\theta z}$ of the cavity edge when degenerated into a circular cavity.

position. When the incident frequency increases to an intermediate frequency with $k_1r = 1.0$, the increase in the DSCF$\sigma^*_{\theta z}$ of the debonded structure is very substantial compared with the low-frequency incidence, and the distribution shape also changes considerably. Regardless of whether the structure is debonded or not, the positions of DSCF$\sigma^*_{\theta z\max}$ are at approximately 20° and 160°. Comparing this with when $k_1r = 0.1$, there is a nearly three times increase in DSCF$\sigma^*_{\theta z\max}$ when debonding occurs and $k_1r = 1.0$. Under the same geological conditions, a debonded concrete inclusion's dynamic response to the intermediate-frequency incident wave is more sensitive, that is, there is a resonance phenomenon between the structure and the site when under intermediate-frequency conditions. When $k_1r = 2.0$, which is a high-frequency incidence, the overall amplitude of DSCF$\sigma^*_{\theta z}$ tends to decrease compared with when $k_1r = 1.0$, but the distribution shape changes radically. The distribution shape of the structure's DSCF$\sigma^*_{\theta z}$ after debonding is obviously different from that when it is not debonded. The DSCF$\sigma^*_{\theta z\max}$ appears at 0° and 180° when the structure is not debonded, and the DSCF$\sigma^*_{\theta z\max}$ appears at 220° and 320° when debonding exists. The overall value of DSCF$\sigma^*_{\theta z}$ is much larger when the structure is debonded than when it is not debonded. Under geological combination A, with an increase in k_1r, the DSCF$\sigma^*_{\theta z}$ of the concrete structure tends to change gradually from low to high and then to low again. When the incident wave is at a high frequency, debonding has the most substantial effect on the distribution shape and the positions of the DSCF maximums of the concrete inclusion.

Figure 4 shows the dynamic stress concentration around the steel inclusion in the sandstone covering layer when the SH wave for geological combination A is perpendicularly incident from the granite layer to the sandstone layer. In this instance, the parameters are $\rho^* = 0.8$, $k^* = 1.5$, $\rho^{\#} \approx 2.8$, and $k^{\#} \approx 1.0$. The density and shear modulus of steel are much larger than those of concrete. It can be concluded that the inclusion's stiffness is greater, and the inclusion is "harder." Compared with what is revealed in Figure 6, the DSCF$\sigma^*_{\theta z}$ in Figure 4 is considerably reduced overall. The reason for this may be that the concrete is relatively soft, and it more easily absorbs more energy under the action of dynamics, where this differs from the concrete inclusion is in that, in addition to high-frequency incident waves, low-frequency incident waves also affect the distribution shape and the maximum positions of the DSCF$\sigma^*_{\theta z}$ for the debonded steel inclusion. When $k_1r = 1.0$ and the structure is not debonded, the positions of DSCF$\sigma^*_{\theta z\max}$ are at about 200° and 340°, and when the structure is debonded, the positions of DSCF$\sigma^*_{\theta z\max}$ are at about 220° and 320°; the value of DSCF$\sigma^*_{\theta z}$ in the debonded area is greater than when the structure is not debonded. When $k_1r = 1.0$, debonded steel inclusions, such as debonded concrete structures, are more sensitive to the dynamic response of intermediate-frequency incident waves, and, overall, DSCF$\sigma^*_{\theta z}$ is greater than when $k_1r = 0.1$ and $k_1r = 2.0$.

Figure 7 illustrates the dynamic stress concentration around the concrete inclusion in the sandstone covering layer when the SH wave for geological combination A is perpendicularly incident from the coal layer to the sandstone layer. In this instance, the SH wave is incident from the softer medium to the harder medium. The parameters are $\rho^* \approx 1.7$, $k^* = 0.4$, $\rho^{\#} \approx 1.6$, and $K^{\#} \approx 0.45$. Compared with what is revealed in Figure 6, the overall decrease in DSCF$\sigma^*_{\theta z}$ shown in Figure 7 is considerable, that is, as the shear modulus of the covering layer increases, the DSCF$\sigma^*_{\theta z}$

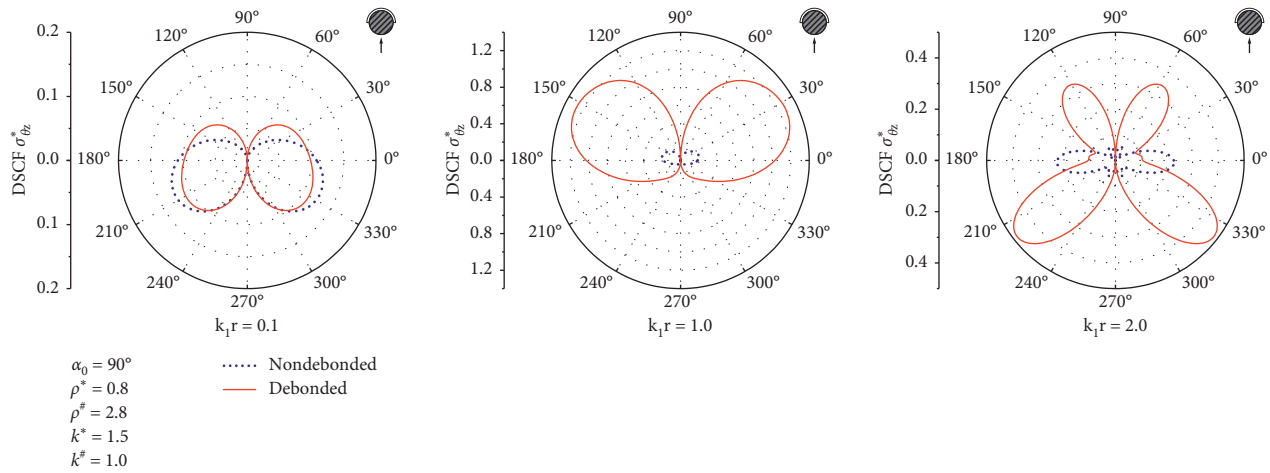

Figure 4: DSCF$\sigma^*_{\theta z}$ of geological combination A with a debonded Q345 steel inclusion.

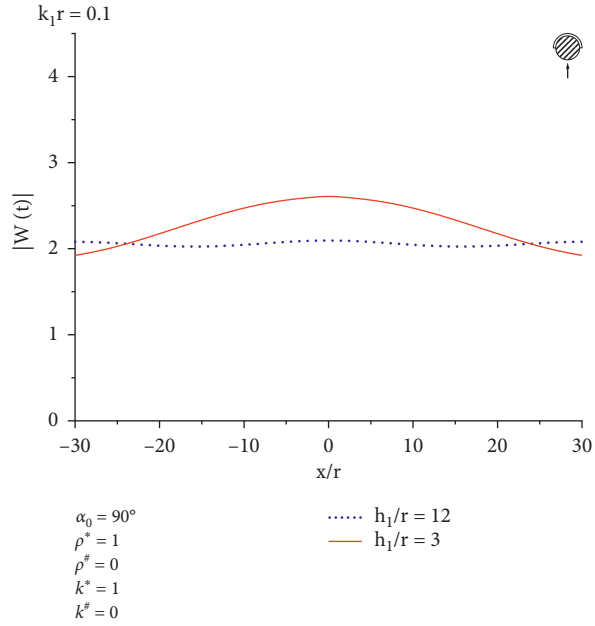

Figure 5: Variation in surface displacement amplitudes $|W^{(t)}|$ with x/r when degenerated into a circular cavity.

of the inclusion in the covering layer tends to decrease. Figure 7 also demonstrates that, as the frequency of the incident wave increases, the overall DSCF$\sigma^*_{\theta z}$ increases gradually. When the incident wave is low frequency or intermediate frequency, whether the structure is debonded or not has little effect on the distribution shape and the positions of the DSCF$\sigma^*_{\theta z\max}$ for the structure. When the incident wave is at a high frequency, the existence of debonding also only slightly changes the overall value of the DSCF$\sigma^*_{\theta z}$, and it does not change the distribution shape. The reason may be that, in such a geological combination, the density of the concrete inclusion and sandstone layers and the wave velocity are relatively close to the parameters of the lower coal layer, and the effect of debonding is not pronounced. In this case, the concrete structure and the sandstone layer are close to forming a whole, and this reveals a simultaneously strong reflection effect for the SH wave transmitted from the lower coal layer; this is the energy barrier effect.

Figure 8 depicts the dynamic stress concentration around the steel inclusion in the sandstone covering layer when the SH wave for geological combination A is perpendicularly incident from the coal layer to the sandstone layer. In this instance, the parameters are $\rho^* \approx 1.7$, $k^* = 0.4$, $\rho^\# \approx 5.2$, and $k^* = 0.3$. Compared with what is shown in Figure 7, the overall value of the DSCF$\sigma^*_{\theta z}$ is greatly reduced, which further confirms the phenomenon that the larger the shear modulus of the inclusion, the smaller the amount of energy absorbed and the smaller the DSCF$\sigma^*_{\theta z}$. It can be seen from Figure 8 that when $k_1 r = 0.1$ and $k_1 r = 2.0$, the DSCF$\sigma^*_{\theta z}$ shape for the steel inclusion in the presence of debonding changes drastically compared with when

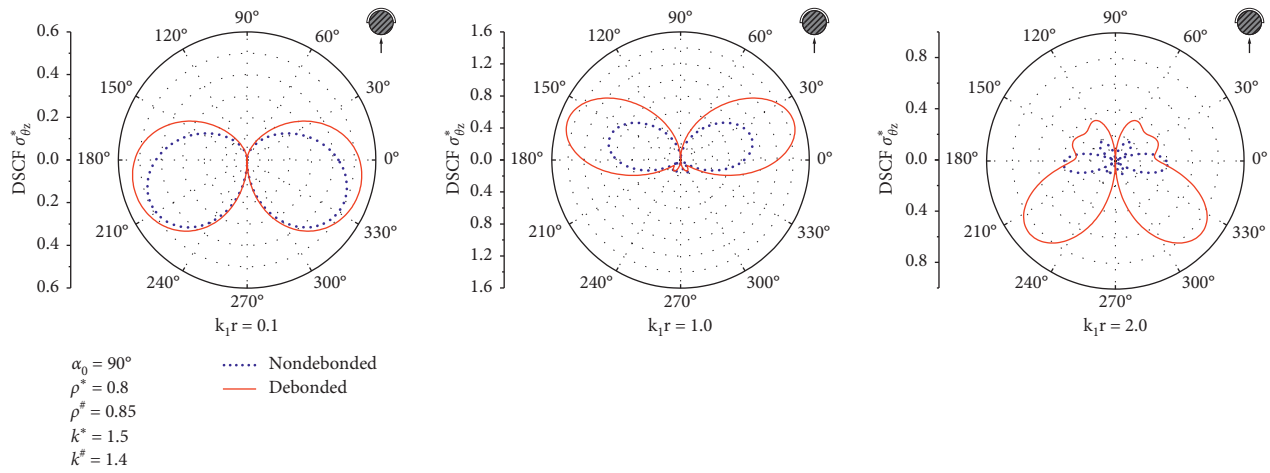

Figure 6: DSCF$\sigma^*_{\theta z}$ of geological combination A with a debonded C30 concrete inclusion.

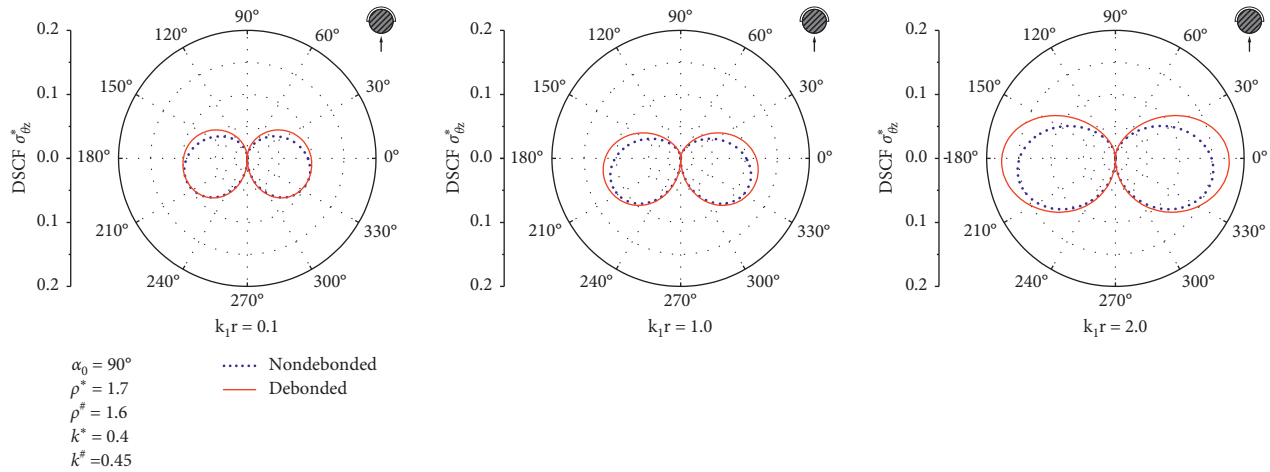

Figure 7: DSCF$\sigma^*_{\theta z}$ of geological combination B with a debonded C30 concrete inclusion.

debonding is absent, and the DSCF$\sigma^*_{\theta z}$ value of the debonded position undergoes a notable increase. When debonding exists in the inclusion and $k_1r = 0.1$, the DSCF$\sigma^*_{\theta z\max}$ positions change to 130° and 50°, and when $k_1r = 2.0$, the DSCF$\sigma^*_{\theta z\max}$ positions change to 160° and 20°. Furthermore, when $k_1r = 1.0$, the shape of the DSCF$\sigma^*_{\theta z}$ of the steel inclusion with debonding is close to that without debonding, and there is a slight increase in the DSCF$\sigma^*_{\theta z}$ for the debonded position. Figures 8 and 7 also demonstrate that, under geological combination B, the change in the frequency of the incident wave has no obvious effect on the DSCF$\sigma^*_{\theta z}$ of a nondebonded steel inclusion, and the impacts of low-frequency and high-frequency SH waves on the debonded steel inclusion are notable.

Figures 9 and 10 identify the changes in the DSCF$\sigma^*_{\theta z\max}$ around the debonded concrete or steel inclusion in the sandstone covering layer in geological combination A in response to incident wave k_1r. In this instance, the parameters $p^* \approx 0.8$ and $K^\# \approx 1.5$ of the covering layer are the same, and the parameters $\rho^\#$ and $K^\#$ of the two inclusions are different. The worth of analyzing this problem lies in finding the frequency bands in which the concrete and steel structures are most sensitive to the dynamic response of the incident waves under the two common geological combinations, which will further provide a theoretical basis for how to reduce the effect of dynamic stress concentration in engineering design. In Figure 9, when there is no debonding of the concrete structure, the DSCF$\sigma^*_{\theta z\max}$ increases gradually along with k_1r, reaches a maximum when $k_1r \approx 0.35$, and then follows a trend of decreasing vibration. When debonding exists, the DSCF reaches the maximum simultaneously when $k_1r \approx 0.35$ and $k_1r \approx 1.1$, and the values of the two are relatively close. Subsequently, DSCF$\sigma^*_{\theta z\max}$ also decreases slowly, but the overall value of the DSCF$\sigma^*_{\theta z\max}$ is still larger than that for the nondebonded structure. This also explains the phenomenon that the DSCF$\sigma^*_{\theta z\max}$ progressively becomes larger first and then becomes smaller, as demonstrated in Figure 6. In Figure 10, the DSCF$\sigma^*_{\theta z\max}$ of the nondebonded steel inclusion is revealed to be smaller than the overall DSCF$\sigma^*_{\theta z\max}$ value for the concrete inclusion, but the trends of the two are closer to each other. In the case of debonded steel inclusion, the DSCF$\sigma^*_{\theta z\max}$ appears only

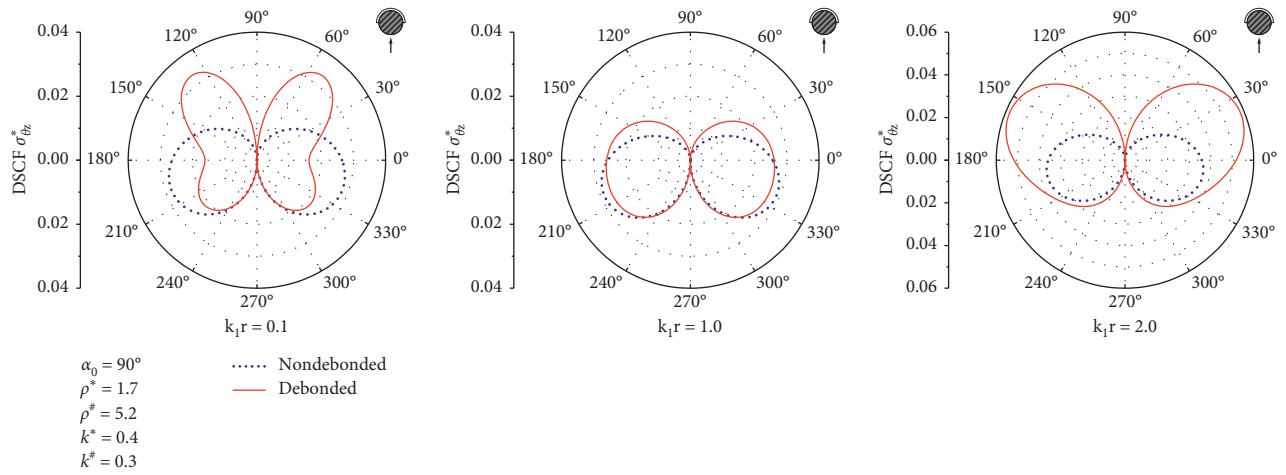

Figure 8: DSCF$\sigma^*_{\theta z}$ of geological combination B with debonded Q345 steel inclusion.

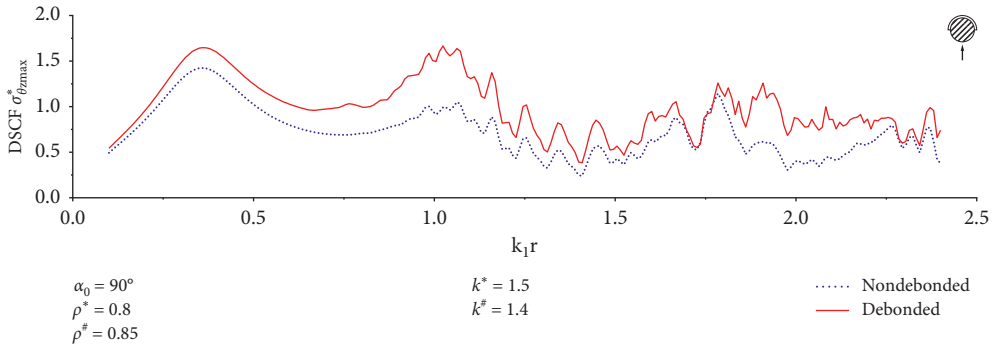

Figure 9: Variation of the DSCF$\sigma^*_{\theta z}$ with $k_1 r$ for geological combination A with debonded C30 concrete inclusion.

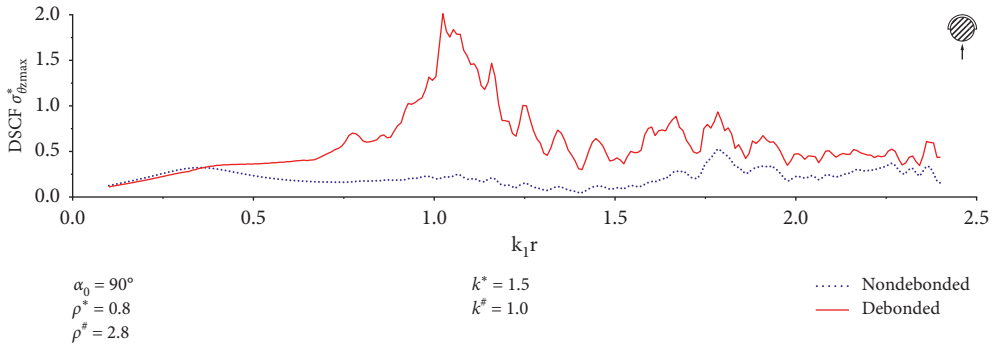

Figure 10: Variation of the DSCF$\sigma^*_{\theta z}$ with $k_1 r$ for geological combination A with debonded Q345 steel inclusion.

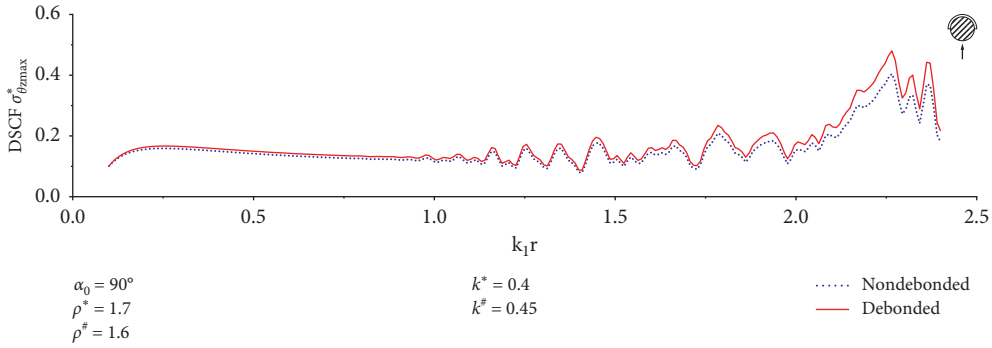

Figure 11: Variation of the DSCF$\sigma^*_{\theta z}$ with $k_1 r$ for geological combination B with debonded C30 concrete inclusion.

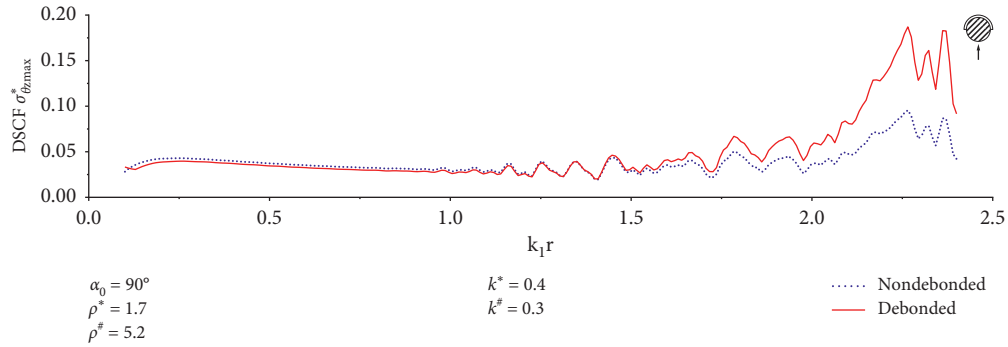

Figure 12: Variation of the DSCF$\sigma^*_{\theta z}$ with k_1r for geological combination B with debonded Q345 steel inclusion.

when $k_1r \approx 1.1$ and then decreases gradually. The overall value of the DSCF$\sigma^*_{\theta z\max}$ is still much larger than that of nondebonded structures. Under the same geological condition, because of utilizing different materials, the dynamic characteristics of the structure are very different. It is therefore essential to take the necessary measures at the design stage to reduce this adverse effect, according to the actual situation and in view of the possible debonding problems.

Figures 11 and 12 depict the changes in the DSCF$\sigma^*_{\theta z\max}$ around the debonded concrete or steel inclusion in the sandstone covering layer with incident wave k_1r in geological combination B. In this instance, the parameters $p* \approx 1.7$ and $k^* = 0.4$ are the same, and the parameters $\rho^\#$ and $K^\#$ of the two inclusions are different. Compared with what is revealed in Figures 9 and 10, Figures 11 and 12 identify that because of the relative increase of the shear modulus of the covering layer with respect to the lower soil layer, the overall value of the DSCF$\sigma^*_{\theta z\max}$ is reduced considerably. The regularity of the change of the DSCF$\sigma^*_{\theta z\max}$ between $k_1r = 0.1$ and $k_1r = 2.0$ illustrated in Figures 11 and 12 can be confirmed by Figures 8 and 9, but the DSCF only becomes close to the maximum when $k_1r = 2.3$. This phenomenon also shows that the dynamic response's sensitive frequency is affected by the parameters for the upper and lower soil media. Under geological combination B, the inclusion's dynamic response to the high-frequency incident wave is more obvious. In Figure 11, because the media parameters of concrete and sandstone are relatively close, it is not obvious whether the structure experiences a change due to debonding. Figure 12 demonstrates that, as the incident wave frequency increases, the increase in the DSCF$\sigma^*_{\theta z\max}$ of the debonded steel inclusion is large, which is consistent with Figure 8.

Figures 13 and 14 show the variation in the ground displacement amplitude $|W^{(t)}|$ with the position x/r when the sandstone covering layer in geological combination A has a debonded concrete or steel inclusion. The horizontal surface displacement is close to a constant when $k_1r = 0.1$. This confirms that when k_1r is relatively small and the wave is incident at a low frequency, the influence of the inclusion on the horizontal displacement of the ground is not sizable, regardless of whether the structure is debonded or not. As the frequency of the incident wave increases, the surface displacement oscillates and presents more obvious dynamic characteristics. The larger the value of k_1r, the more severe the surface displacement shock. The presence or absence of debonding at an inclusion has a prodigious effect on ground displacement. When $k_1r = 1.0$, the surface displacement near a nondebonded concrete or steel inclusion increases considerably, but the oscillation amplitude is small, and the maximum increase is close to 4.5. When the inclusion is debonded, the closer to the inclusion, the greater the reduction in surface displacement. When $k_1r = 2.0$, the response of a nondebonded concrete inclusion to ground displacement is not large, whereas the surface displacement near a steel inclusion increases slightly.

Figures 15 and 16 identify the variation of the ground displacement amplitude $|W^{(t)}|$ with the position x/r when the sandstone covering layer in geological combination B has a debonded concrete or steel inclusion. When $k_1r = 0.1$, the amplitude of the ground surface displacement far away from the inclusion location is close to 2.0, and there is only an incident wave and a reflected wave in a half space. The sum of the amplitudes of the two is 2.0, which is essentially consistent. The closer to the inclusion, the larger the amplitude of the surface displacement. Compared with Figures 13 and 14, Figures 15 and 16 show that the medium parameters of different soil layers are dissimilar, and the influence of the presence of an inclusion on surface displacement is also different. As the frequency of the incident wave increases, the amplitude of the surface displacement also increases, but the overall amplitude of the surface displacement of geological combination B is reduced substantially compared with geological combination A, which also shows that the soft covering layer is effective with respect to surface displacement. It has a magnifying effect, whereas the covering layer with a large shear modulus has a reducing effect on the ground surface displacement. When $k_1r = 1.0$, the two curves in Figures 15 and 16 are effectively the same, which indicates that, in this case, the presence of debonding at the inclusion has little effect on the amplitude of the surface displacement. When $k_1r = 2.0$, so the fre-

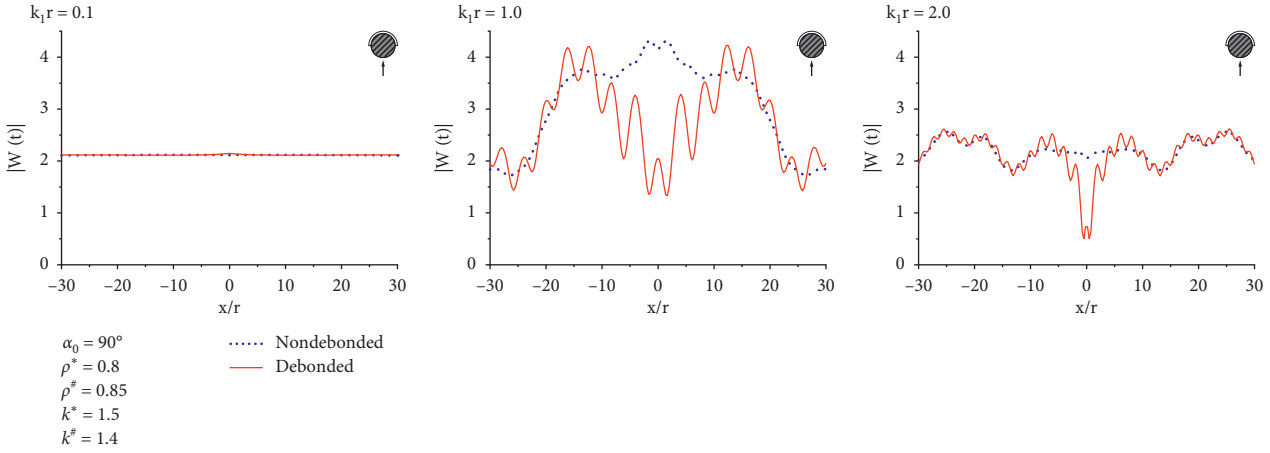

Figure 13: Variation of surface displacement amplitudes $|W^{(t)}|$ with x/r for geological combination A with debonded C30 concrete inclusion.

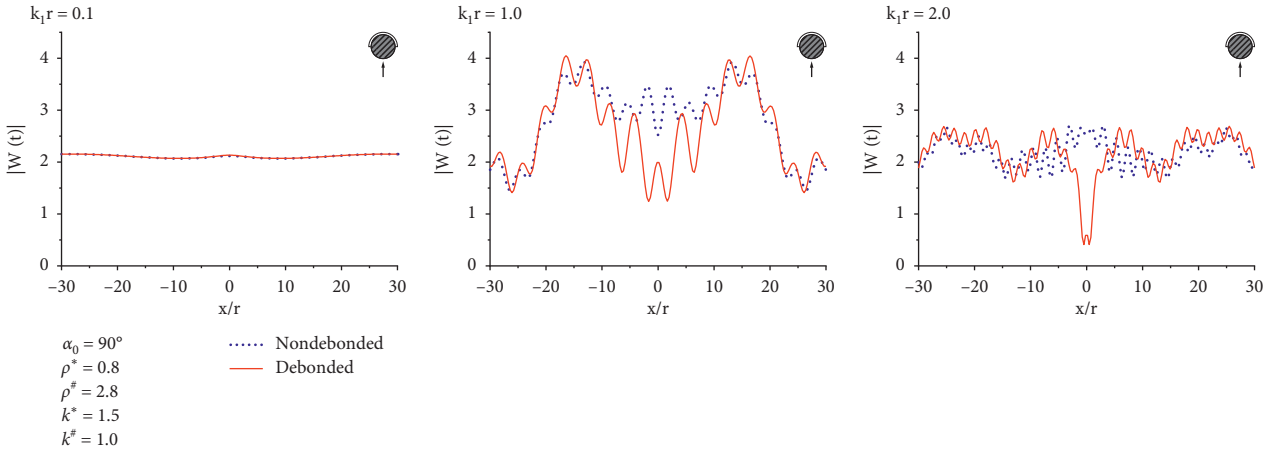

Figure 14: Variation of surface displacement amplitudes $|W^{(t)}|$ with x/r for geological combination A with debonded Q345 steel inclusion.

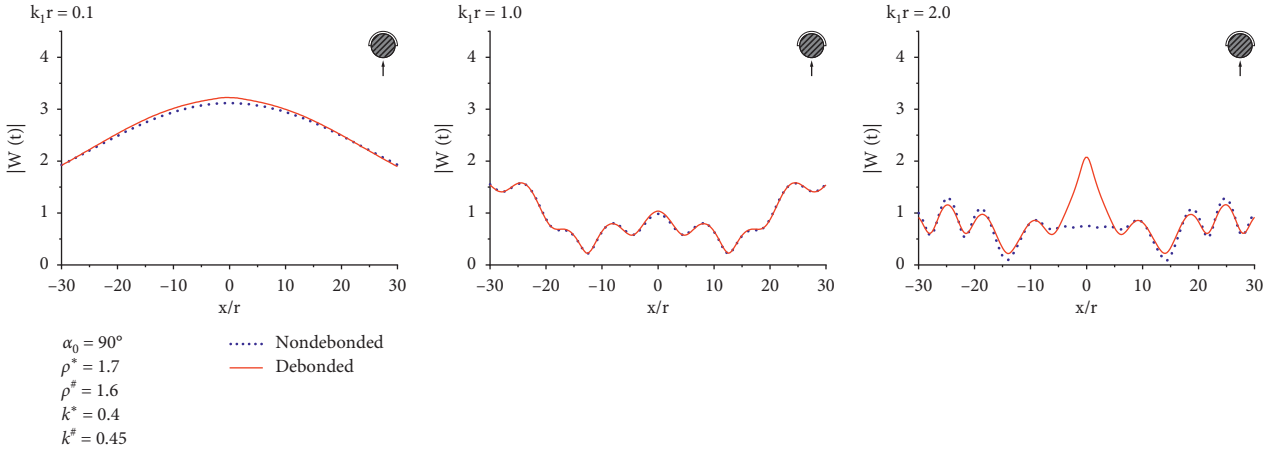

Figure 15: Variation of surface displacement amplitudes $|W^{(t)}|$ with x/r for geological combination B with debonded C30 concrete inclusion.

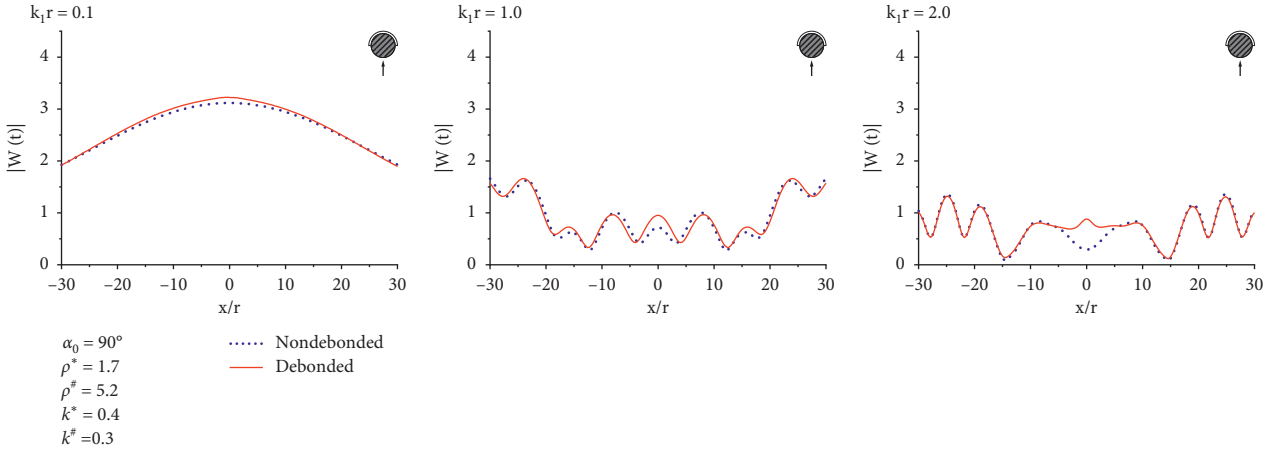

FIGURE 16: Variation of surface displacement amplitudes $|W^{(t)}|$ with x/r for geological combination B with debonded Q345 steel inclusion.

quency of the incident wave is high, the debonded inclusion amplifies the displacement of the nearby surface.

6. Conclusions

This paper has obtained analytical solutions to the problem of SH wave scattering by a cylindrical inclusion with partial debonding in the covering layer. Furthermore, it has used numerical examples to analyze the effects of debonding on the dynamic stress concentration and surface displacement of a concrete or steel inclusion under two geological combinations. The following conclusions have been drawn.

The soft cover layer has a relatively obvious amplification effect on the DSCF$\sigma^*_{\theta z\max}$ and $|W^{(t)}|$, whereas the hard covering layer has a reflection and energy shielding effect on SH waves.

The smaller the shear modulus of the inclusion, relative to the soil medium, the larger the DSCF$\sigma^*_{\theta z\max}$ and $|W^{(t)}|$.

When comparing the problem of SH wave scattering in a half space with SH wave scattering in a covering layer, the combination of the parameters for the soil layer mediums and the inclusion is more complicated. When a structure in a soft covering layer is debonded, it is more sensitive to the dynamic response of incident waves at low and intermediate frequencies and has a greater impact on the DSCF$\sigma^*_{\theta z\max}$ and $|W^{(t)}|$. When a structure in a hard covering layer is debonded, it is more sensitive to the dynamic response of incident waves at high frequencies and has a greater impact on the DSCF$\sigma^*_{\theta z\max}$ and $|W^{(t)}|$.

The parameters of the different soil layer mediums and the inclusion, the frequency of the incident wave, and the presence or absence of debonding at the inclusion all affect the DSCF around the structure and the horizontal surface displacement. Therefore, engineering designs should consider the influence of various factors in combination with different geological conditions.

Data Availability

The data used to support the findings of this study are included within the article.

Conflicts of Interest

The authors declare that there are no conflicts of interest regarding the publication of this paper.

Acknowledgments

This work was supported by the Fundamental Research Funds for Central Universities (3072019CF0205).

References

[1] Y. M. A. Hashash, J. J. Hook, B. Schmidt, and J. I-Chiang Yao, "Seismic design and analysis of underground structures," *Tunnelling and Underground Space Technology*, vol. 16, no. 4, pp. 247–293, 2001.

[2] Y.-H. Pao, C.-C. Mow, and J. D. Achenbach, "Diffraction of elastic waves and dynamic stress concentrations," *Journal of Applied Mechanics*, vol. 40, no. 4, pp. 213–219, 1973.

[3] J.-w. Liang, L.-j. Yan, and V. W. Lee, "Effects of a covering layer in a circular-arc canyon on incident plane SV waves," *Acta Seismologica Sinica*, vol. 14, no. 6, pp. 660–675, 2001.

[4] J.-w. Liang, L.-J. Yan, and V. W. Lee, "Scattering of plane P waves by circular-arc layered alluvial valleys: an analytical solution," *Acta Seismologica Sinica*, vol. 14, no. 2, pp. 176–195, 2001.

[5] M. Baron and A. Matthews, "Diffraction of a pressure wave by a cylindrical cavity in an elastic medium," *Journal ofApplied Mechanics*, vol. 28, no. 3, pp. 205–207, 1961.

[6] C. C. Mow and L. J. Mente, "Dynamic stresses and displacements around cylindrical discontinuities due to plane harmonic shear waves," *Journal of Applied Mechanics*, vol. 30, no. 4, pp. 598–604, 1963.

[7] D. Liu, B. Gai, and G. Tao, "Applications of the method of complex functions to dynamic stress concentrations," *Wave Motion*, vol. 4, no. 3, pp. 293–304, 1982.

[8] H. Lin and D. Liu, "Scattering of SH-wave around a circular cavity in half space," *Earthquake Engineering and Engineering Vibration*, vol. 22, pp. 9–16, 2002.

[9] D. Liu and H. Lin, "Scattering of SH-waves by a shallow buried cylindrical cavity and the ground motion," *Explosion and Shock Waves*, vol. 23, pp. 6–12, 2003.

[10] H. Qi and J. Yang, "Dynamic analysis for circular inclusions of arbitrary positions near interfacial crack impacted by SH-

wave in half-space," *European Journal of Mechanics-A/solids*, vol. 36, pp. 18–24, 2012.

[11] J. Yang and H. Qi, "The scattering of steady-state SH waves in a bi-material half space with multiple cylindrical elastic inclusions," *Waves in Random and Complex Media*, vol. 29, no. 1, pp. 162–177, 2019.

[12] O. Coussy, "Scattering of elastic waves by an inclusion with an interface crack," *Wave Motion*, vol. 6, no. 3, pp. 223–236, 1984.

[13] Y. Yang and A. N. Norris, "Shear wave scattering from a debonded fibre," *Journal of the Mechanics and Physics of Solids*, vol. 39, no. 2, pp. 273–294, 1991.

[14] A. Norris and Y. Yang, "Dynamic stress on a partially bonded fiber," *Journal of Applied Mechanics*, vol. 58, no. 2, pp. 404–409, 1991.

[15] Y.-S. Wang and D. Wang, "Scattering of elastic waves by a rigid cylindrical inclusion partially debonded from its surrounding matrix-I. SH case," *International Journal of Solids and Structures*, vol. 33, no. 19, pp. 2789–2815, 1996.

[16] Y.-S. Wang, Z.-Y. Qiu, and G.-L. Yu, "Scattering of SH waves from a partially debonded rigid elliptic cylinder," *Soil Dynamics and Earthquake Engineering*, vol. 21, no. 2, pp. 139–149, 2001.

[17] P.-S. Yang, S.-W. Liu, and J.-C. Sung, "Transient response of SH waves in a layered half-space with sub-surface and interface cracks," *Applied Mathematical Modelling*, vol. 32, no. 4, pp. 595–609, 2008.

[18] H. Cao and V. W. Lee, "Scattering of plane SH waves by circular cylindrical canyons with variable depth-to-width ratio," *European Journal of Earthquake Engineering*, vol. 3, p. 29~37, 1989.

[19] H. Cao and V. W. Lee, "Scattering and differaction of plane P waves by circular cylindrical canyons with variable depth-to-width ratio," *Soil Dynamics and Earthquake Engineering*, vol. 9, no. 3, pp. 141–150, 1990.

[20] V. W. Lee and J. Karl, "Diffraction of SV waves by underground, circular, cylindrical cavities," *Soil Dynamics and Earthquake Engineering*, vol. 11, no. 8, pp. 445–456, 1992.

[21] H. P. Brandow and V. Lee, "Scattering and diffraction of plane P-waves in a 2-D elastic half-space II: shallow arbitrary shaped canyon," *Earthquake Engineering and Engineering Vibration*, vol. 16, no. 3, pp. 459–485, 2017.

[22] C.-S. Zhu, X.-Q. Fang, J.-X. Liu, and H.-Y. Li, "Surface energy effect on nonlinear free vibration behavior of orthotropic piezoelectric cylindrical nano-shells," *European Journal of Mechanics-A/Solids*, vol. 66, pp. 423–432, 2017.

[23] X.-Q. Fang, T.-F. Zhang, B.-L. Li, and R.-J. Yuan, "Elastic-slip interface effect on dynamic stress around twin tunnels in soil medium subjected to blast waves," *Computers and Geotechnics*, vol. 119, Article ID 103301, 2020.

[24] C. Zhu, X. Fang, and J. Liu, "A new approach for smart control of size-dependent nonlinear free vibration of viscoelastic orthotropic piezoelectric doubly-curved nanoshells," *Applied Mathematical Modelling*, vol. 77, pp. 137–168, 2020.

[25] X. Pan, H. Su, C. Sun, and Y. Hong, "The behavior of crack initiation and early growth in high-cycle and very-high-cycle fatigue regimes for a titanium alloy," *International Journal of Fatigue*, vol. 115, pp. 67–78, 2018.

[26] X. Pan and Y. Hong, "High-cycle and very-high-cycle fatigue behaviour of a titanium alloy with equiaxed microstructure under different mean stresses," *Fatigue & Fracture of Engineering Materials & Structures*, vol. 42, no. 9, pp. 1950–1964, 2019.

[27] X. Pan, G. Qian, S. Wu, Y. Fu, and Y. Hong, "Internal crack characteristics in very-high-cycle fatigue of a gradient structured titanium alloy," *Scientific Reports*, vol. 10, Article ID 4742, 2020.